

EFFECT OF THERMOMECHANICAL PROCESSING ON MICROSTRUCTURE AND MECHANICAL PROPERTIES IN AN Al-Cu-Mg-Si ALLOY

*M. Gazizov^{1,2}, J. K. Sunde¹, S. Wenner³, R. Holmestad¹, and R. Kaibyshev²

¹ *Department of Physics, Norwegian University of Science and Technology (NTNU), Trondheim, Norway*
(*Corresponding author: marat.gazizov@ntnu.no)

² *Belgorod State University, Belgorod, Russia*

³ *SINTEF Industry, Trondheim, Norway*

ABSTRACT

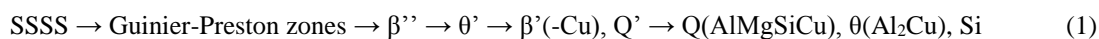
Mechanical properties and microstructure of an Al-4.7Cu-0.74Mg-0.51Si-0.48Mn-0.10Cr-0.09Ti-0.02Fe (wt. %) alloy subjected to various thermomechanical processing (TMP) have been investigated and compared to conventional ageing at 170°C (designated T6). Three TMP routes involving cold deformation of solution treated samples were tested. These were (i) 3%-stretching (T8-3%), (ii) equal-channel angular pressing (ECAP) to true strain (ϵ) of ~ 1 (T8-1) and (iii) ECAP to $\epsilon \sim 2$ (T8-2), all with subsequent ageing at 170°C for 0-96 h. At peak age conditions, both yield stress, ultimate tensile strength and elongation-to-fracture decreased for the T8-3% state as compared to the T6 condition. Intermediate ECAP (T8-1 and T8-2) lead to significant increase in maximum yield stress, ultimate tensile strength and elongation-to-fracture. The changes in mechanical properties were related to microstructure evolution, encompassing changes in grain sizes, dislocation densities, precipitate morphology and phase fractions, which were characterised using transmission electron microscopy. Relations between TMP, precipitation behavior and contributions to different strengthening mechanisms are evaluated.

KEYWORDS

Al-Cu-Mg-Si alloy, Thermomechanical processing, Mechanical properties, Microstructure, Precipitation, Transmission electron microscopy, Fractography

INTRODUCTION

Al-Cu-Mg-Si alloys are widely used as structural materials in aerospace industry due to their attractive combination of high specific strength, good fracture toughness and enhanced creep resistance. These properties are largely due to the formation of a large number of nano-sized metastable precipitates during artificial ageing (Polmear, 2006; Eskin, 2003; Gazizov, Dubina, Zhemchuzhnikova, & Kaibyshev, 2015). The precipitation behaviour in these alloys is complicated and depends among other things on Cu concentration and the Mg:Si ratio (Wolverton, 2001; Chakrabarti, & Laughlin, 2004). In general, the precipitation sequence has been presented in a prior study (Eskin, 2003) as follows:



where SSSS stands for supersaturated solid solution, which is reached after quenching from solution heat treatment.

It is known that cold deformation prior to ageing affects the precipitation sequence, kinetics and composition, as well as particle morphology and distribution. This is due to changes in the density of crystallographic defects such as vacancies, grain boundaries and dislocations, which act as sites for solute segregation and heterogeneous nucleation of different phases (Porter, Easterling, & Sherif, 2009; Gazizov et al., 2015). The density of these defects could be changed in the alloy by the cold deformation level. An opportunity to increase the intermediate deformation level has emerged in recent years by use of equal-channel angular pressing (ECAP) (Polmear, 2006; Valiev & Langdon, 2006; Gazizov, Malopheyev, & Kaibyshev, 2014). However, reports on the efficiency of this thermomechanical processing (TMP) route in strengthening of the aluminum alloys are scarce (Gazizov et al., 2015; Muñoz-Morris & Morris, 2011; Huang, Robson, & Prangnell, 2010). An additional increase in specific strength of Al-Cu-Mg-Si alloys by TMP techniques involving large plastic deformations followed by ageing can expand the range of applications for this alloy system in the aircraft industry, and replace existing load-bearing units by more lightweight alternatives.

The aim of the present study is to estimate the potential for producing Al-Cu-Mg-Si alloys with higher strength using various TMPs involving solution heat treatment, quenching and intermediate cold deformation followed by artificial ageing. Herein, the microstructure and mechanical properties of the Al-Cu-Mg-Si alloy were investigated after various TMP routes with 3%-stretching (T8-3%), ECAP to a true strain (ϵ) of ~ 1 (T8-1) and ~ 2 (T8-2). Results obtained for cold worked conditions were compared with the alloy after conventional ageing (T6).

EXPERIMENTAL

Aluminum alloy ingots with chemical composition Al-4.9Cu-0.74Mg-0.51Si-0.48Mn-0.1Cr-0.08Ti-0.02Fe (wt. %) were prepared by casting. The ingots were homogenized at 500°C for 24 h followed by cooling to room temperature in a furnace. Subsequently, the ingots were rolled at $\sim 400^\circ\text{C}$ with a reduction of $\sim 60\%$, forming plates with a thickness of 14 mm. Rods with dimensions 14 mm \times 14 mm \times 80 mm and sheets with 1.5 mm thickness were cut from the central part of these plates and solution heat treated at 500°C for 1 h followed by water quenching. These samples were processed to four different conditions (Figure 1). In the first condition, designated T6, the sheets with 1.5 mm thickness were artificially aged with no pre-straining (Figure 1a). In the second condition, designated T8-3%, the sheets were machined to produce flat “dog-bone” tensile samples with 16 mm gauge length and 3 \times 1.5 mm cross-section to simulate stretching. The sample axis matched with the direction of the previous hot rolling. The samples were tensioned at room temperature using initial strain rates of $\sim 2.1 \times 10^{-3} \text{ s}^{-1}$ up to a fixed plastic strain of 3% (or true strain of ~ 0.03), followed by similar artificial ageing conditions (Figure 1b). For the third and fourth conditions, designated T8-1 and T8-2, the 14 mm \times 14 mm \times 80 mm rods were subjected to ECAP at room temperature to true strains of ~ 1 and ~ 2 , respectively (Figure 1b). ECAP was conducted using a die having channels with a square internal cross-section of 14 mm \times 14 mm and intersecting at an angle of 90° (Figure 1c). Deformation through these configurations of channels produces a strain of ~ 1 on

each passage through the die (Valiev et al., 2006). In the T8-2 condition, the rod was rotated 90° between passes. The duration of one pass was ~3 min. In all material conditions, artificial aging was conducted at 170°C for 0–96 h in a chamber furnace with air circulation.

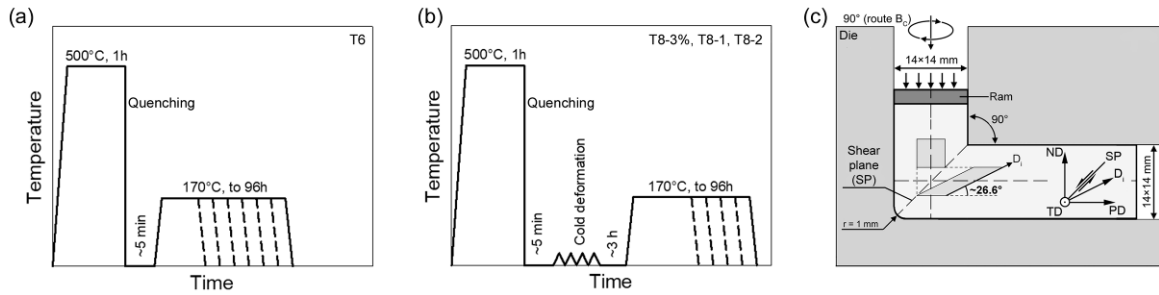


Figure 1. Scheme of the heat treatments in (a) non-deformed (T6 condition) and (b) deformed conditions (T8-3% and T8-1/T8-2). (c) Scheme of the die in ECAP used in this study.

The hardness measurements were performed on cross-sectional surfaces of the samples cut longitudinally to the hot rolling direction in T6 condition, stretching direction in T8-3% condition and pressing direction in T8-1 and T8-2 conditions. A Wilson Wolpert 402 MVD hardness tester with a constant load of 5 N and loading time of 10 s was used. At least ten indentations in arbitrarily selected areas were used for each data point in order to determine the average value and standard deviation of the Vicker's hardness (HV_{0.5}) for each condition. The tensile tests were performed using an Instron 5882 testing machine at ambient temperature and an initial strain rate of $\sim 2.1 \times 10^{-3} \text{ s}^{-1}$ on flat specimens with a gauge length of ~16 mm and 3 mm × 1.5 mm cross-section after ageing. These specimens were cut with the tensile axis parallel to the hot rolling and pressing directions for the T6 and T8-1/T8-2 conditions, respectively. For each material condition, two tensile tests were conducted, and the yield stress (YS), ultimate tensile strength (UTS), uniform elongation (δ_{UE}) and elongation-to-failure (δ) were determined by averaging. Uniform elongations were estimated as plastic strain corresponding to the loss of stability by Considère's criterion ($d\sigma/d\varepsilon = \sigma$) when necking sets in (Yasnikov, Estrin, & Vinogradov, 2017). The samples for microstructural examination were cut from the central area of the hot-rolled plates, stretched samples and ECAPed rods, parallel to the rolling, stretching and pressing directions, respectively. Metallographic analysis was performed using an Olympus GX71 optical microscope after grinding, mechanical polishing and etching of samples by standard Keller's reagent. A mean linear intercept method was used to measure the average grain size. The fracture surfaces were examined using a FEI Quanta 600FEG scanning electron microscope (SEM). For transmission electron microscopy (TEM), the samples were prepared through grinding with abrasive papers and subsequent electropolishing at -30°C in a solution of 1/3 nitric acid and 2/3 methanol using a Tenupol-5 twinjet polishing unit. Microstructure and crystal orientation maps (OM) in the samples were analyzed by a 200 kV JEOL 2100F microscope equipped with a precession electron diffraction (PED) system (NanoMEGAS, ASTAR). Scanning PED was performed using a precession angle of 1°, 1 nm beam size (unprocessed) and a 6.4 nm step size. The subsequent indexation, orientation mapping and visualization were carried out using the ASTAR MapViewer and Index software (Rauch, Portillo, Nicolopoulos, Bultreys, Rouvinov, & Moeck, 2010), as well as the MTEX software. In order to use reliable orientation data, the OMs were filtered using a reliability index over 25.

RESULTS AND DISCUSSION

Mechanical Properties

Figure 2a shows the hardness curves for the alloy in T6, T8-3%, T8-1 and T8-2 conditions after ageing for 0-96 h. The hardness of the as-quenched specimen was approximately ~83 HV_{0.5}. During artificial ageing, the hardness of the non-deformed samples increased gradually to a peak of ~169 HV_{0.5} at 16 h. For T8-3% ($\varepsilon \sim 0.03$), the ageing response in the under-ageing stage (up to ~7 h) is quite similar to the

T6 condition. It is interesting to note that further ageing leads to formation of a plateau with lower hardness value ($\sim 157 \text{ HV}_{0.5}$) than the T6 condition. In the over-ageing stage, the hardness of the T8-3% sample decreases in a similar manner as the T6 condition, showing consistently lower hardness values. It is speculated that the result of a lower maximum hardness value and hardness curve broadening (or double peak hardness evolution) can be related to the delay of- and/or acceleration of nucleation of strengthening particles of different metastable phases.

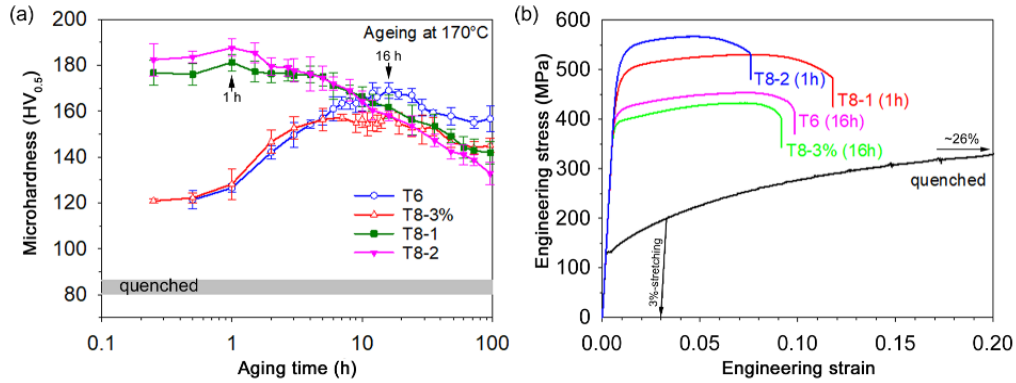


Figure 2. (a) Vicker's hardness as a function of ageing time for the T6, T8-3%, T8-1 and T8-2 conditions. Black arrows show alloy conditions studied by TEM. (b) σ - ϵ curves for the alloys in peak aged states.

It is seen that ECAP is more efficient in strengthening the alloy than 3% stretching. The hardness of the alloy after ECAP to true strains of $\sim 1/\sim 2$ and short ageing for 0.25 h is higher than the alloy in peak-aged T6 conditions. Ageing for 1 h leads to slight increases in hardness to peak values of $\sim 181.3 \text{ HV}_{0.5}$ and $\sim 187.6 \text{ HV}_{0.5}$ for the T8-1 and T8-2 conditions, respectively. In the over-ageing stage, the hardness of the ECAPed samples decreases faster than in the T6 or T8-3% conditions. The hardness values for ECAPed samples after 20 h of ageing are quite similar to that in the peak-ageing stage of the T8-3% condition, whereas after 96 h ageing, the T8-1 and T8-2 samples demonstrate lower hardness as compared to T8-3%.

Table 1. Tensile properties of the alloy in different peak aged conditions

Condition	YS (MPa)	UTS (MPa)	δ_{UE} (%)	δ (%)	YS/UTS ratio
As-quenched	126 ± 4	343 ± 3	21.5 ± 1.5	26.2 ± 1.8	0.38
T6 (16h)	407 ± 3	452 ± 2	6.4 ± 0.3	9.8 ± 0.8	0.90
T8-3% (16 h)	392 ± 2	432 ± 2	6.3 ± 0.2	8.7 ± 0.2	0.91
T8-1 (1 h)	465 ± 4	530 ± 2	7.3 ± 0.8	12.4 ± 1.8	0.88
T8-2 (1 h)	508 ± 4	563 ± 6	4.6 ± 1.0	7.6 ± 1.1	0.90

The typical engineering stress-strain (σ - ϵ) curves and tensile properties of the alloy in peak ageing stages are shown in Figure 2b. The σ - ϵ curves are typical for peak-aged aluminum alloys with a high YS/UTS ratio (~ 0.9). Limited strain hardening takes place after yielding, and an apparent steady state is attained after a small strain. A significant uniform elongation (δ_{UE}) appears (Table 1). The YS and UTS values for the alloy in the peak ageing stage correlate well with the hardness measurements. It is interesting to note that the alloy in the T8-1 condition demonstrates higher ductility (δ), whereas a second pass of ECAP leads to significant decrease of this value. It seems that crystallographic texture and/or structural heterogeneity have a significant effect on tensile properties of the ECAPed samples (Valiev et al., 2006).

Microstructure

Optical micrographs (Figure 3) and OMs (Figure 4) show the microstructure of the alloy in T6, T8-1 and T8-2 conditions. The point-to-point ($\Delta\theta$) and the cumulative point-to-origin ($\Sigma\Delta\theta$) misorientations developed along the highlighted lines in the deformation microstructure developed during ECAP to strain of ~ 1 and ~ 2 are shown in Figure 5. In T6 condition, grains are elongated in shape with dimensions of $87 \pm$

23 μm and $35 \pm 10 \mu\text{m}$ in the rolling and transverse directions, respectively (Figure 3a). Coarse particles of several equilibrium phases are observed. The distribution of these particles is non-uniform with an average volume fraction of $\sim 2.4\%$. In the T8-3% condition an increase in dislocation density is observed, but no obvious change of grain structure takes place.

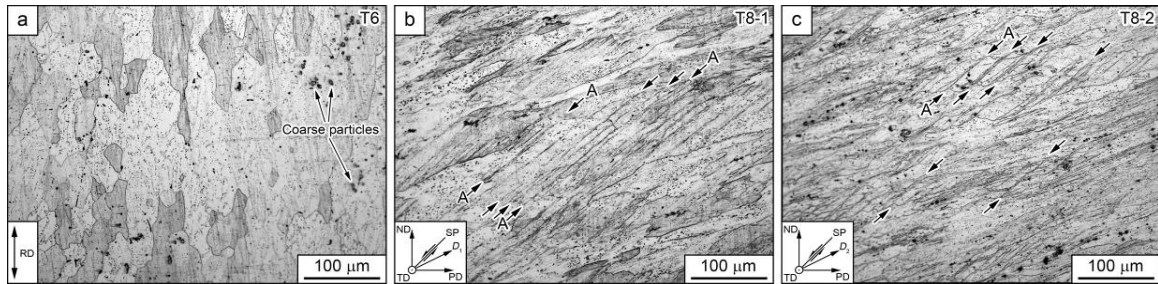


Figure 3. Optical micrographs of the alloy in (a) T6, (b) T8-1 and (c) T8-2 conditions. Numerous deformation bands are marked “A”. Sample orientation is related with scheme of the die in ECAP (Figure 1c).

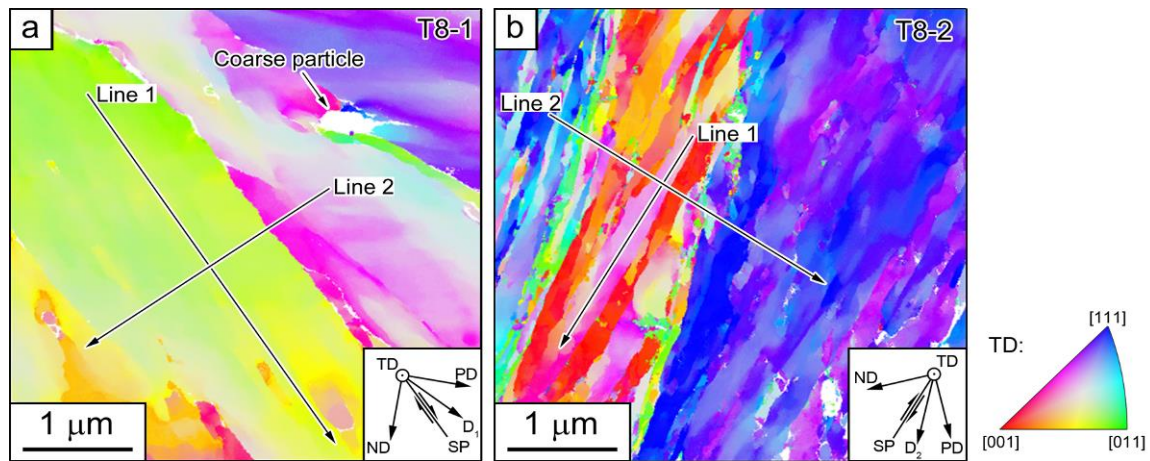


Figure 4. Representative OMs in TD plane for the alloy in (a) T8-1 and (b) T8-2 conditions. Sample orientation is related with scheme of the die in ECAP (Figure 1c).

ECAP results in elongation of initial grains in D_i directions (where i is number of ECAP passes) and development of fibrous microstructures, which are aligned roughly parallel to the shear plane (SP) or shear direction. At $\varepsilon \sim 1$, such fibrous structures are heterogeneously developed in some initial grain interiors due to formation of numerous deformation bands (DB), which are marked “A” in Figure 3b. These DBs are entirely delimited by low-angle boundaries (LAB) with misorientations less than 15° (Line 2, Figures 4a and 5b). A continuous change of $\Sigma\Delta\theta$ within DBs (Line 1, Figures 4a and 5a) indicates a deformation gradient in those locations, suggesting a high density of tensor dislocations and deformation heterogeneity. After $\varepsilon \sim 2$ deformation became less homogeneous. The shear bands are the main characteristic features of the deformation structure and the density of DBs (marked “A”) increases (Figures 3c and 4b). A continuous change of $\Sigma\Delta\theta$ within the DBs is also observed (Line 1, Figures 4b and 5c). However, these DBs are delimited by high-angle boundary (HAB) misorientations above 15° (Line 2, Figures 4b and 5d).

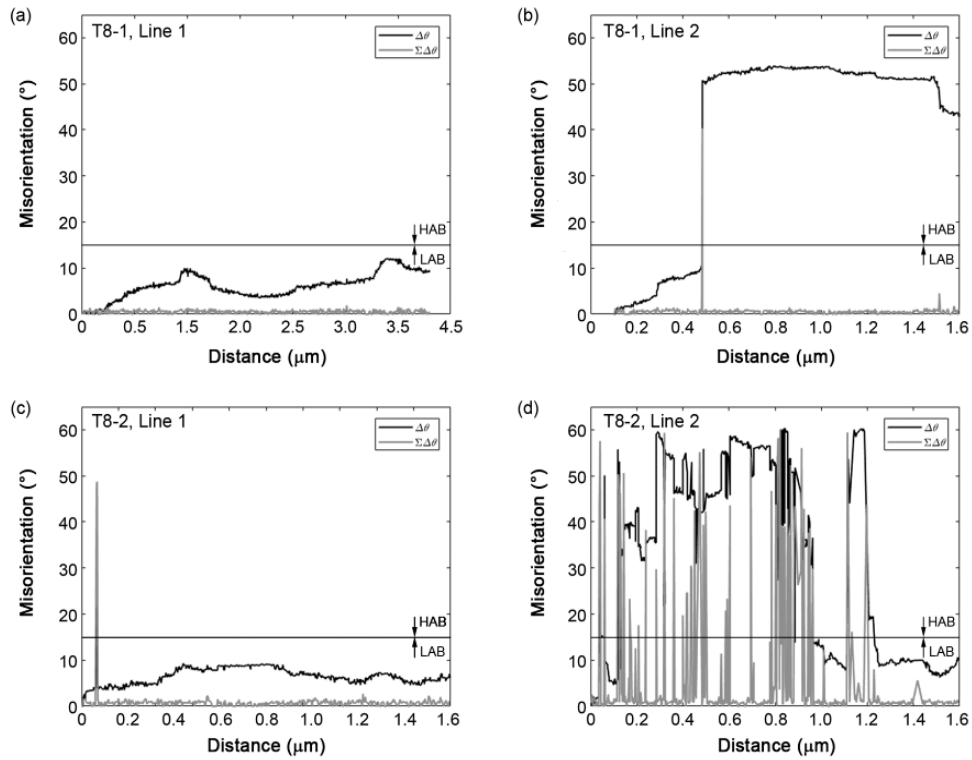


Figure 5. Point-to-point ($\Delta\theta$) and point-to-origin ($\Sigma\Delta\theta$) misorientation profiles along Line 1 and Line 2 highlighted in Figure 4 for the alloy in (a, b) T8-1 and (c, d) T8-2 conditions.

The microstructure of the alloy after 1 and 16 h of ageing was investigated by TEM (the respective ageing times are indicated by arrows in the hardness curves in Figure 2a). Representative bright- and dark-field TEM images are shown in Figure 6. In T6 and T8-3% conditions the TEM images along $[001]_{Al}$ and $[011]_{Al}$ zone-axes were analyzed, however only the $[001]_{Al}$ images are shown here. Three types of precipitates were classified based on morphological features. The first type is coarse plate-shaped precipitates which are identified as the semi-coherent θ' -phase (Wenner, Friis, Marioara, Andersen, & Holmestad, 2015). This phase is common in Al-Cu-Mg-Si alloys with high Cu content (Eskin, 2003; Gazizov et al., 2015). The second type is needle-shaped precipitates. Dark spots represent cross-sections of these precipitates in the viewing direction in the bright-field TEM images. In the T8-3% condition, heterogeneous nucleation and growth of plate- and needle-shaped precipitates take place along dislocation lines. The third type is lath-shaped precipitates, which are uniformly distributed in the Al matrix, and have significantly lower volume fractions compared to volume fractions of the plates and/or needles. These laths are likely the L-phase, observed predominantly in Al-Mg-Si alloys with Cu additions (Chakrabarti, & Laughlin, 2004; Marioara, Andersen, Stene, Hasting, Walmsley, Van Helvoort, & Holmestad, 2007). Thus, in peak-aged T6 and T8-3% conditions, the essential contribution of precipitation strengthening to the overall strength of the alloy is provided by plate- and needle-shaped precipitates. We therefore conclude that a 3%-stretching affects negatively on the distribution and morphology of particles, leading to a decrease in the overall strength of the alloy after peak ageing. This is in spite of the increased contribution to structural strengthening by dislocations (Gazizov & Kaibyshev, 2017; Saito, Marioara, Røyset, Marthinsen, & Holmestad, 2014) compared to the T6 condition.

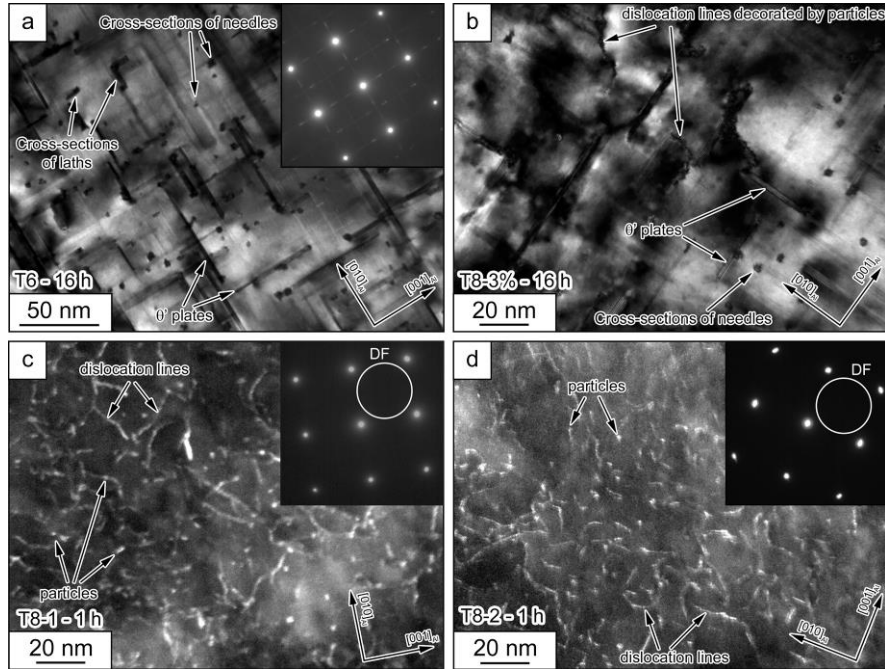


Figure 6. Bright field TEM images of the alloy in (a) T6 and (b) T8-3% conditions after ageing for 16 h. Dark-field TEM images of the alloy in (c) T8-1 and (d) T8-2 conditions after 1 h ageing.

Dark-field TEM images obtained from regions free from DBs are shown in Figures 6c and 6d for the alloy in peak-aged T8-1 and T8-2 conditions, respectively. The electron beam was parallel to the $[001]_{Al}$ zone-axis. Analysis of TEM images shows that the heterogeneous nucleation and growth of strengthening particles predominantly take place along dislocation lines after short-time ageing. These particles look like needle-shaped precipitates in peak-aged T6 and/or T8-3% conditions in $[001]_{Al}$ dark field TEM images (Figures 6c and 6d). However, these “needles” are shorter in length than the ones in the T6 and/or T8-3% conditions. Thus, the microstructure contains DBs delimited by LABs and HABs and a high density of dislocations, which are pinned by dispersed particles, providing a high strength state for the alloy after ECAP.

SEM images (Figure 7) show fractured surface morphologies of the samples after tensile tests for the alloy in peak-aged T6, T8-3%, T8-1 and T8-2 conditions. It shows that the fractures of the alloy occur in a ductile manner with formation of dimples having round shape in T6 and T8-3% conditions (Figures 7a and 7b, respectively). In Figure 7c, the shallow dimples and coarse particles are responsible for the failure in the T8-1 condition. However, two fracture modes can be distinguished in T8-2 condition (Figure 7d). The first has smooth areas of brittle transgranular fractures. This is attributed to the DBs, which are inclined to the pressing direction (Figure 1c). The second has rough areas with shallow dimples, which are responsible for fracture occurring in a relatively ductile manner. These fracture modes agree with the structural heterogeneity for the alloy in T8-2 condition.

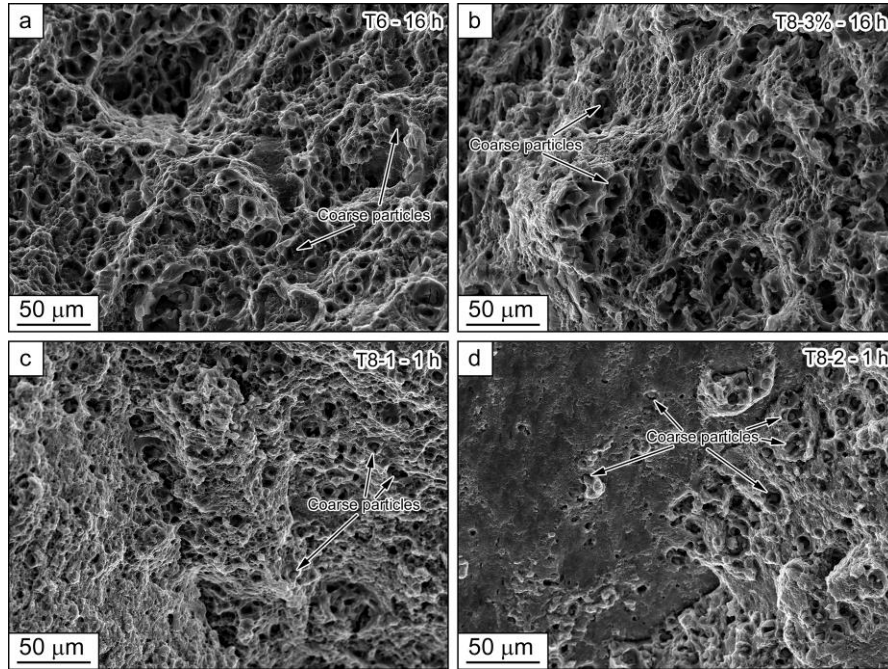


Figure 7. SEM images of the fracture surfaces for the alloy in (a) T6-16h (b), T8-3%-16h, (c) T8-1-1h and (d) T8-2-1h conditions.

CONCLUSIONS

The Al-4.7Cu-0.74Mg-0.51Si-0.48Mn-0.10Cr-0.09Ti-0.02Fe (wt. %) alloy was subjected to various TMPs involving 3%-stretching (T8-3%) and ECAP to true strains of ~ 1 (T8-1) and ~ 2 (T8-2), followed by aging at 170°C for 0–96 h. The mechanical properties and microstructure were investigated and compared to conventional ageing at 170°C (T6).

- 1) Yield stress (YS), ultimate tensile strength (UTS) and elongation-to-fracture (δ) decreased from ~ 407 MPa, ~ 452 MPa and $\sim 9.8\%$ in peak-aged T6 condition to ~ 392 MPa, ~ 432 MPa and $\sim 8.7\%$ in T8-3% condition, respectively. Intermediate ECAP to $\epsilon \sim 1/\epsilon \sim 2$ led to an increase in maximum YS to $\sim 465/\sim 508$ MPa and UTS to $\sim 530/\sim 563$ MPa, and δ values attained were $\sim 12.4/\sim 7.6\%$, respectively.
- 2) In peak-aged T6 and T8-3% conditions, the essential contribution of precipitation strengthening to overall strength of the alloy is provided by plate- and rod-shaped particles. The 3%-stretching affects negatively on distribution and morphology of particles and leads to a decrease in the overall strength of the alloy after peak aging compared to the T6 condition, despite the increase in contribution of structural strengthening by dislocations. The high strength of ECAPed samples is attributed to structural strengthening by the DBs delimited by LABs and HABs, as well as the high density of dislocations, which are pinned by dispersed particles.

ACKNOWLEDGMENTS

This work is financially supported by the Faculty of Natural Sciences at the Norwegian University of Science and Technology [NTNU] (Project No. 81617879) and The Ministry of Education and Science and Council on grants of the President of the Russian Federation (Grant No. MK-957.2018.8). The TEM work was carried out on the NORTEM infrastructure (Grant 197405) at NTNU, Trondheim, Norway. The authors are grateful to the staff of the TEM Gemini Center at NTNU and the Joint Research Center at Belgorod State University for their assistance with the structural and mechanical characterisations.

REFERENCES

- Chakrabarti, D.J., & Laughlin D.E. (2004). Phase relation and precipitation in Al-Mg-Si alloys with Cu additions. *Progress in Materials Science*, 49, 389–410. [https://doi.org/10.1016/S0079-6425\(03\)00031-8](https://doi.org/10.1016/S0079-6425(03)00031-8)
- Eskin, D.G. (2003). Decomposition of supersaturated solid solutions in Al-Cu-Mg-Si alloys. *Journal of Materials Science*, 38, 279–290. <https://doi.org/10.1023/A:1021109514892>.
- Gazizov, M., Malopheyev, S., & Kaibyshev, R. (2014). The effect of second-phase particles on grain refinement during equal-channel angular pressing in an Al-Cu-Mg-Ag alloy. *Journal of Materials Science*, 50(2), 990–1005. <https://doi.org/10.1007/s10853-014-8659-4>.
- Gazizov, M.R., Dubina A.V., Zhemchuzhnikova, D.A., & Kaibyshev, R.O. (2015) Effect of equal-channel angular pressing and aging on the microstructure and mechanical properties. *The Physics of Metals and Metallography*, 116(7), 718–729. <https://doi.org/10.1134/S0031918X15070066>.
- Gazizov, M., & Kaibyshev, R. (2017). Precipitation structure and strengthening mechanisms in an Al-Cu-Mg-Ag alloy. *Materials Science and Engineering A*, 702, 29–40. <https://doi.org/10.1016/j.msea.2017.06.110>
- Huang, Y., Robson, J.D., & Prangnell, P.B. (2010). The formation of nanograin structures and accelerated room-temperature theta precipitation in a severely deformed Al-4 wt.% Cu alloy. *Acta Materialia*, 58, 1643–1657. <https://doi.org/10.1016/j.actamat.2009.11.00>.
- Marioara, C.D., Andersen, S.J., Stene, T.N., Hasting, H., Walmsley, J., Van Helvoort, A.T.J., & Holmestad, R. (2007). The effect of Cu on precipitation in Al-Mg-Si alloys. *Philosophical Magazine*, 87, 3385–3413. <https://doi.org/10.1080/14786430701287377>.
- Muñoz-Morris, M.A., & Morris, D.G. (2011). Microstructure control during severe plastic deformation of Al-Cu-Li and the influence on strength and ductility. *Materials Science and Engineering A*, 528, 3445–3454. <https://doi.org/10.1016/j.msea.2011.01.036>.
- Polmear, I.J. (2006). *Light alloys. From traditional alloys to nanocrystals* (4nd ed.) Oxford: Butterworth-Heinemann (Elsevier).
- Porter, D.A., Easterling, K.E., & Sherif, M. (2009). *Phase Transformations in Metals and Alloys* (3rd ed.) New York: CRC Press.
- Rauch, E.F., Portillo, J., Nicolopoulos, S., Bultreys, D., Rouvinov, S., & Moeck, P. (2010). Automated nanocrystal orientation and phase mapping in the transmission electron microscope on the basis of precession electron diffraction. *Zeitschrift für Kristallographie*, 225, 103–109. <https://doi.org/10.1524/zkri.2010.1205>.
- Saito, T., Marioara, C.D., Røyset, J., Marthinsen, K., & Holmestad, R. (2014). The effects of quench rate and pre-deformation on precipitation hardening in Al-Mg-Si alloys with different Cu amounts. *Materials Science and Engineering A*, 609, 72–79. <https://doi.org/10.1016/j.msea.2014.04.094>.
- Valiev, R.Z., & Langdon, T.G. (2006). Principles of equal-channel angular pressing as a processing tool for grain refinement. *Progress in Materials Science*, 51(7), 881–981. <https://doi.org/10.1016/j.pmatsci.2006.02.003>

- Wenner, S., Friis, J., Marioara, C.D., Andersen, S.J., & Holmestad, R. (2015). Structural modifications and electron beam damage in aluminium alloy precipitate θ^{\prime} -Al₂. *Philosophical Magazine*, 95(31), 3524–3534. <https://doi.org/10.1080/14786435.2015.1090639>
- Wolverton, C. (2001). Crystal structure and stability of complex precipitate phases in Al-Cu-Mg-(Si) and Al-Zn-Mg alloys. *Acta Materialia*, 49, 3129–3142. [https://doi.org/10.1016/S1359-6454\(01\)00229-4](https://doi.org/10.1016/S1359-6454(01)00229-4).
- Yasnikov, I.S., Estrin, Y., & Vinogradov, A. (2017). What governs ductility of ultrafine-grained metals? A microstructure based approach to necking instability. *Acta Materialia*, 141, 18–28. <https://doi.org/10.1016/j.actamat.2017.08.069>.